

Coherent 3D Scene Diffusion From a Single RGB Image

Manuel Dahnert¹Angela Dai¹Norman Müller²Matthias Nießner¹¹Technical University of Munich, Germany²Meta Reality Labs Zurich, Switzerland

Abstract

We present a novel diffusion-based approach for coherent 3D scene reconstruction from a single RGB image. Our method utilizes an image-conditioned 3D scene diffusion model to simultaneously denoise the 3D poses and geometries of all objects within the scene. Motivated by the ill-posed nature of the task and to obtain consistent scene reconstruction results, we learn a generative scene prior by conditioning on all scene objects simultaneously to capture the scene context and by allowing the model to learn inter-object relationships throughout the diffusion process. We further propose an efficient surface alignment loss to facilitate training even in the absence of full ground-truth annotation, which is common in publicly available datasets. This loss leverages an expressive shape representation, which enables direct point sampling from intermediate shape predictions. By framing the task of single RGB image 3D scene reconstruction as a conditional diffusion process, our approach surpasses current state-of-the-art methods, achieving a 12.04% improvement in AP_{3D} on SUN RGB-D and a 13.43% increase in F-Score on Pix3D.

1 Introduction

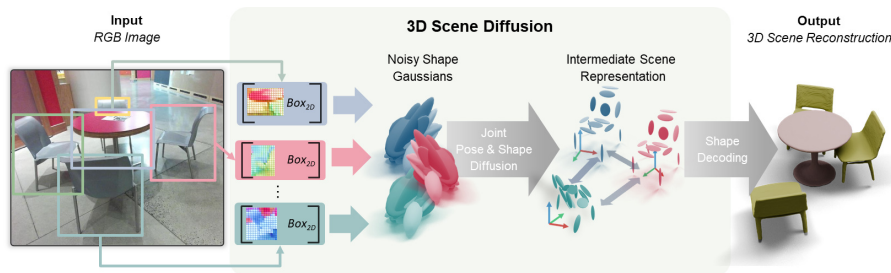


Figure 1: Given a single RGB image of an indoor scene, our model reconstructs the 3D scene by jointly estimating object arrangements and shapes in a globally consistent manner. Our novel diffusion-based 3D scene reconstruction approach achieves highly accurate predictions by utilizing a novel generative scene prior that captures scene context and inter-object relationships, and by employing an efficient surface alignment loss formulation for joint pose- and shape-synthesis.

Holistic 3D scene understanding is crucial for various fields and lays the foundation for many downstream tasks in robotics, 3D content creation, and mixed reality. It bridges the gap between 2D perception and 3D understanding. Despite impressive advancements in 2D perception and 3D reconstruction of individual objects [56, 5, 12, 38], 3D scene reconstruction from a single RGB observation remains a challenging problem due to its ill-posed nature, heavy occlusions, and the

complex multi-object arrangements found in real-world environments. While previous works [15, 32, 33] have shown promising results, they often recover 3D shapes independently and thus do not leverage the scene context nor inter-object relationships. This leads to unrealistic and intersecting object arrangements. Additionally, common feed-forward reconstruction methods [48, 77, 37] struggle with heavy occlusions and weak shape priors, resulting in noisy or incomplete 3D shapes, which hinders immersion and hence limits the applicability in downstream tasks. To address these challenges and to advance 3D scene understanding, we propose a novel generative approach for coherent 3D scene reconstruction from a single RGB image. Specifically, we introduce a new diffusion model that learns a generative scene prior capturing the relationships between objects in terms of arrangement and shapes. When conditioned on a single image, this model simultaneously reconstructs poses and 3D geometries of all scene objects. By framing the reconstruction task as a conditional synthesis process, we achieve significantly more accurate object poses and sharper geometries. Publicly available 3D datasets [47, 62] typically only provide partial ground-truth annotations, which complicates joint training of shape and pose. To overcome this, we propose a novel and efficient surface alignment loss formulation $\mathcal{L}_{\text{align}}$ that enables joint training of shape and pose even under the lack of full ground-truth supervision. Unlike previous methods [48, 77] that involve costly shape decoding and point sampling on the reconstructed surface, our approach employs an expressive intermediate shape representation that enables direct point sampling from the conditional shape prior. This provides additional supervision and results in more globally consistent 3D scene reconstructions. Our method not only outperforms current state-of-the-art methods by 12.04% in AP_{3D}¹⁵ on SUN RGB-D [62] and by 13.43% in F-Score on Pix3D [64] but also generalizes to other indoor datasets without further fine-tuning.

In summary, our contributions include:

- A novel diffusion-based 3D scene reconstruction approach that jointly predicts poses and shapes of all visible objects within a scene.
- A novel way for modeling a generative scene prior by conditioning on all scene objects simultaneously to capture scene context and inter-object relationships.
- An efficient surface alignment loss formulation $\mathcal{L}_{\text{align}}$ that leverages an expressive intermediate shape representation for additional supervision, even in the absence of full ground-truth annotation.

2 Related Works

The task of 3D scene reconstruction from a single view combines the fundamental domains of 2D perception and 3D modeling into a unified challenge of holistic 3D understanding. Given the multi-faceted nature of the task, we are providing a comprehensive overview of the relevant research directions and contextualizing our contributions.

2.1 Single-View 3D Reconstruction

Object Reconstruction. Since the foundational work by Roberts [54], numerous methods have been developed to learn cues for deriving 3D object structures, thereby bridging the gap between 2D perception and the 3D world. These methods typically involve an image encoder network that processes the input image of a single object, capturing its features. The extracted features are either correlated with an encoded shape database to retrieve a suitable shape [32, 33, 17], or used by a 3D decoder to reconstruct the object in a specific 3D representation, such as voxel grids [8, 72], point clouds [14, 43], meshes [70, 66], or neural fields [73, 27]. [19] uses a message-passing graph network between geometric primitives to reason about the structure of the shape.

Scene Reconstruction. Early works formulated single-view scene reconstruction as 3D scene completion from given or estimated depth information [63, 10, 78, 9] in a volumetric grid. While these methods have produced promising results, their representational power to model fine details is limited by the spatial resolution of the 3D grid. Multi-object reconstruction and scene parsing methods represented objects using primitives [13, 23], voxel grids [68, 35, 52], or CAD models [26, 24], while also considering the relation between the objects [31]. The approach presented by Nie *et allet@tokeneonedot* [48] is particularly relevant, proposing a holistic method for joint pose and shape estimation from a single image. Zhang *et allet@tokeneonedot* [77] extended this idea by

incorporating an implicit shape representation and an additional pose refinement using a graph neural network. Although these methods provided significant advances in holistic scene understanding, they struggled with accurate pose estimation and produced noisy scene objects, leading to intersecting or incomplete objects. In contrast to these previous works, we are proposing a generative method to obtain a strong scene prior and formulate the reconstruction task as a conditional synthesis task. This allows for more robust reconstruction that is less prone to object intersections or implausible object geometries.

2.2 3D Diffusion Models

In recent years, denoising diffusion probabilistic models (DDPMs) have emerged as a versatile class of generative models, demonstrating impressive results in image and video generation. Unlike other classes of generative models such as auto-regressive models [46, 75, 59], Generative Adversarial Networks (GANs) [71, 79] and Variational Autoencoders (VAEs), diffusion models iteratively reverse a Markovian noising process. This method ensures stable training and has the ability to capture diverse modes while producing detailed outputs. Several approaches have utilized diffusion models to learn the distribution of individual 3D shapes using various 3D representations, including volumetric grids [6, 7, 25], point clouds [42, 74], meshes [2], implicit functions [30], neural fields [45, 58, 29] or hybrid representations [80, 76]. [53] propose a hierarchical voxel diffusion model, which is capable of modelling large-scale and fine-detailed geometry. While these methods can synthesize high-quality 3D shapes, they typically focus on single objects in canonical space. In contrast, we are proposing a diffusion-based approach that addresses the more challenging problem of multi-object scene reconstruction, encompassing accurate pose estimations and an understanding of inter-object relationships.

Conditional Diffusion for 3D Reconstruction. Recent works also use diffusion models for single-view object reconstruction [6, 7, 44]. For instance, [65] learns the shape distribution of a single category by denoising a set of 2D images for each object, while [44] projects image features onto noisy point clouds during the diffusion process to ensure geometric plausibility. Recently, several works proposed to leverage multi-view consistency within pre-trained text-conditional 2D image diffusion models to reconstruct individual 3D objects [38, 51, 57]. Similar to our work, Tang *et al* [67] use a diffusion model to learn scene priors from synthetic data, showing unconditional scene synthesis of a single room type and text-conditional generation. However, their approach does not support image-based scene reconstruction. Furthermore, it depends on clean synthetic data, which provides full 3D ground truth supervision and CAD model retrieval, thereby limiting shape diversity. While these existing methods have shown promising results on single objects or synthetic scenes, our approach targets real-world scenes. By framing the reconstruction task as a conditional generation process, our scene prior accurately delivers poses and shapes of multiple objects, even in the presence of strong occlusions, significant clutter, and challenging lighting conditions.

3 Method

3.1 Overview

Our method takes a single RGB image of an indoor scene as input and generates a globally consistent 3D scene reconstruction that matches the input image. To this end, we are framing the reconstruction task as a conditional generation problem using a diffusion model conditioned on the input view (Sec. 3.2), which simultaneously predicts the poses (Sec. 3.3) and shapes (Sec. 3.4) of all objects in the scene. Given the ill-posed nature of single-view reconstruction, such a probabilistic formulation is particularly well-suited for this task. To ensure accurate reconstructions and to learn a strong scene prior, we model inter-object relationships within the scene using an intra-scene attention module (Sec. 3.5). Additionally, recognizing the incomplete ground truth in many 3D indoor scene datasets, we introduce a loss formulation for joint shape and pose training, which enables training under only partially available supervision (Sec. 3.6). An overview of our approach is illustrated in Fig. 1. In the following sections, we describe each individual contribution in more detail.

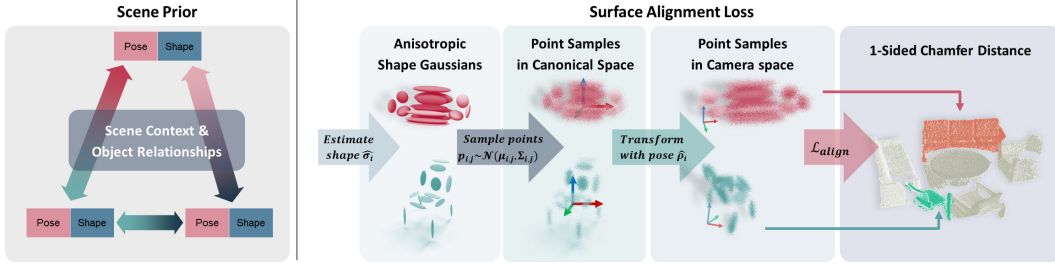


Figure 2: **Scene Prior and Surface Alignment Loss Overview.** (Left) We propose a novel way to model scene priors (Sec. 3.5) by modeling the scene context and the relationships between all objects during the denoising process. (Right) For additional supervision and joint training, we use a surface alignment loss (Sec. 3.6) between a given ground truth depth map and point samples directly drawn from the intermediate shape representation $\hat{\sigma}_i$ and transformed to camera space with the predicted object pose $\hat{\rho}_i$.

3.2 Conditional 3D Scene Diffusion

We frame the scene reconstruction task as a conditional generation process via a diffusion formulation [22]. Given an instance-segmented RGB image \mathbf{I} containing a variable number of 2D objects b_i for $i \in \{1, \dots, n\}$, our model Φ simultaneously estimates all 3D objects $\mathbf{o}_i = (\rho_i, \sigma_i)$ with 7-DoF poses ρ_i and 3D geometries σ_i :

$$(\hat{\mathbf{o}}_1, \dots, \hat{\mathbf{o}}_n) = \Phi(\mathbf{I} | (\mathbf{b}_1, \dots, \mathbf{b}_n)). \quad (1)$$

During the *forward process*, we gradually add Gaussian noise to a data point x_0 to x_T over a series of discrete time steps T . For a given data point x_0 , *e.glet@tokenonedot*, shapes σ_i and poses ρ_i , the noisy version x_t at time step t is given by a Markovian process [22, 60] $q(x_t | x_{t-1})$ and its joint distribution $q(x_{1:T} | x_0)$ can be expressed as:

$$q(x_t | x_{t-1}) = \mathcal{N}(x_t; \sqrt{1 - \beta_t} x_{t-1}, \beta_t \mathbf{I}), \quad (2)$$

$$q(x_{1:T} | x_0) = \prod_{i=1}^T q(x_i | x_{i-1}) \quad (3)$$

with $t \in [1, T]$ and β_t a pre-defined linear variance schedule.

During the *reverse process*, the denoising network Φ tries to remove the noise and recover x_0 from x_T as $p_\Phi(x_{t-1} | x_t, y)$

$$p_\Phi(x_{t-1} | x_t, y) = \mathcal{N}(x_{t-1}; \mu_\Phi(x_t, t, y), \Sigma_\Phi(x_t, t, y)), \quad (4)$$

$$p_\Phi(x_{0:T} | y) = p_\Phi(x_T) \prod_{t=1}^T p_\Phi(x_{t-1} | x_t, y) \quad (5)$$

with y being the conditional information from the input image \mathbf{I} .

Conditioning. To effectively guide the diffusion process $p_\Phi(x_{0:T} | y)$, it is crucial to accurately model the conditional information y . First, we encode the input image \mathbf{I} using a 2D backbone Θ_I and apply 2D instance segmentation to get n detected 2D objects b_i , comprising of its 2D bounding box, image feature patch, and semantic class (cls). Each element is encoded using a specific embedding function Θ . The per-instance y_i and scene condition y is then formed as:

$$y_i = \text{concat}(\Theta_{\text{box}}(\text{box}_i), \Theta_{\text{feat}}(\text{feat}_i), \Theta_{\text{cls}}(\text{cls}_i)), \quad (6)$$

$$y = (y_1, \dots, y_n). \quad (7)$$

To learn a scene prior over all objects in the scene, we condition the denoising network on the scene condition y . This not only enables learning the individual object representations o_i but also facilitates learning to capture the scene context and inter-object relationships (Sec. 3.5). Furthermore, we adopt classifier-free guidance [21] for our model by dropping the condition y with probability $p = 0.8$, *i.elet@tokenonedot*, using a special 0-condition \emptyset . This allows our model to function as a conditional model $p_\Phi(x_0 | y)$ and unconditional model $p_\Phi(x_0)$ at the same time, thus enabling unconditional synthesis (Appendix B).

Loss Formulation. Unlike related works like [23, 48, 77] that regress object poses ρ_i and shape parameters σ_i using a multitude of highly-tuned losses, we train our model Φ to minimize simple diffusion and alignment losses:

$$\mathcal{L}_{\text{joint}}(\mathbf{I}) = \mathcal{L}_{\text{pose}}(\mathbf{I}) + \mathcal{L}_{\text{shape}}(\mathbf{I}) + \lambda \mathcal{L}_{\text{align}}, \quad (8)$$

$$\mathcal{L}_{\text{pose}}(\mathbf{I}) = \mathbb{E}_{\epsilon \sim \mathcal{N}(0,1), t} \|\hat{\epsilon}_\rho(\tilde{\rho}(t), t, \mathbf{I}, \mathbf{b}) - \epsilon\|, \quad (9)$$

$$\mathcal{L}_{\text{shape}}(\mathbf{I}) = \mathbb{E}_{\epsilon \sim \mathcal{N}(0,1), t} \|\hat{\epsilon}_\sigma(\tilde{\sigma}(t), t, \mathbf{I}, \mathbf{b}) - \epsilon\|, \quad (10)$$

where we define $\tilde{z}(t) = \sqrt{\bar{\alpha}_t}z + \sqrt{1 - \bar{\alpha}_t}\epsilon$ for $z \in \{\rho, \sigma\}$ with pre-defined noise coefficients $\bar{\alpha}_t$, while $\hat{\epsilon}_z$ denotes the predicted noise. We use $\lambda = 0.01$ to balances the effect of $\mathcal{L}_{\text{align}}$.

Due to the lack of full ground truth supervision in publically available 3D datasets, we introduce an additional alignment loss $\mathcal{L}_{\text{align}}$ for joint training of pose and shape (Sec. 3.6). Depending on the availability of ground-truth data (see Sec. 4.2, we mask out individual losses.

3.3 Object Pose Parameterization

We adopt the object pose parameterization of [23], defining the pose $\rho_i = (c_i, s_i, \theta_i)$ of an object by its 3D center $c_i \in \mathbb{R}^3$, the spatial size $s_i \in \mathbb{R}^3$, and orientation $\theta_i \in [-\pi, \pi)$ in . The 3D center c_i is further represented by the 2D offset $\delta_i \in \mathbb{R}^2$ between the 2D bounding box center coordinate and the projected coordinate of the 3D center on the image plane, along with the distance $d_i \in \mathbb{R}$ from the object center to the projected center. Our model learns to denoise this 7-dim. pose representation.

3.4 Shape Encoding

We represent object shapes using the disentangled shape representation from [20]. A shape is represented as a shape code $\sigma_i \in \mathbb{R}^{256}$ which is factorized into a set of g oriented, anisotropic 3D Gaussians $G_j, j \in \{1, \dots, g\}$ and an associated 512-dim. latent feature vector per Gaussian. Each Gaussian consist of 16 main parameters: $\mu_j \in \mathbb{R}^3$ (center), factorized covariance matrix $U_j \in \mathbb{R}^{3 \times 3}$ (rotation), $\lambda_j \in \mathbb{R}^3$ (scale) and $\pi_j \in \mathbb{R}^1$ (“mixing” weight). We use $g = 16$ Gaussians to form a scaffolding of the shape’s geometry. Together with their latent features, these Gaussians are decoded into high-fidelity occupancy fields, and the final mesh is extracted by applying marching cubes [40].

While similar to [30], our model learns to denoise this shape parameterization σ_i , our additional surface alignment loss $\mathcal{L}_{\text{align}}$ (Sec. 3.6) provides relational signal between predicted shapes and poses. This enables additional guidance in the face of missing joint pose and shape annotations as in SUN RGB-D dataset [62].

3.5 Scene Prior Modeling

Given the ill-posed nature of single-view reconstruction, a robust scene prior is essential for achieving good performance. Effectively capturing the scene context and modeling the relationships between objects within the scene is crucial for learning this strong scene prior [31, 77]. Previous methods either reconstruct each object individually [15] or refine their features using graph networks [77]. In contrast, our approach considers the entire scene by conditioning on all scene objects simultaneously $p_\Phi(x_0|y)$ and $y = (y_1, \dots, y_N)$ and additionally allows objects to exchange relational information throughout the entire process. We model the inter-object relationships using an attention formulation [69], which has proven to be powerful for aggregating contextual information.

We denote this formulation as Intra-Scene Attention (ISA), which allows all objects within the scene to attend to each other, effectively modeling their relationships. Please refer to Appendix E for more details and to Tab. 2 for the corresponding ablation study, which demonstrates the effectiveness of our learned scene prior.

3.6 Surface Alignment Loss

Publically available 3D scene datasets often only provide partial ground-truth annotations [47, 62]. To facilitate joint training of our model on pose and shape estimation, even in the absence of complete ground-truth annotations, we propose to leverage our expressive intermediate shape representation

to provide additional supervision and to align shapes efficiently with the available partial depth information \mathcal{D} . An illustration of the surface alignment loss formulation is provided in Fig. 2. During training, for each object o_i , we use the expected shape code $\hat{\sigma}_i$ estimation by our model to obtain the predicted Gaussian $\hat{G}_{i,j}$ distribution. Given this scaffolding representation, we directly sample $m = 1000$ points $p_{(j,l)} \sim \mathcal{N}(\mu_j, \Sigma_j)$ per Gaussian $\hat{G}_{i,j}$ resulting in a shape point cloud $P_i = \{p_{(j,l)} | j \in \{1, \dots, g\}, l \in \{1, \dots, m\}\}$. We transform the resulting shape points P_i into the camera frame by the predicted object pose $\hat{\rho}_i$. Using the instance segmentations and ground-truth depth maps, we obtain K_i surface points q_k^i for object o_i and define the surface alignment loss for all visible objects as 1-sided Chamfer Distance [16, 48]

$$\mathcal{L}_{\text{align}} = \frac{1}{n} \sum_{i=1}^n \frac{1}{K_i} \sum_{k=1}^{K_i} \min_{p \in P_i} \|q_k^i - p\|_2^2. \quad (11)$$

Unlike previous works such as [48] that perform costly sampling of points on the decoded shape surface, our approach enables direct point sampling from the conditional shape prior $\hat{G}_{i,j}$. This loss formulation facilitates joint training of pose and shape for all objects simultaneously and its efficacy is demonstrated through ablation studies in Tab. 2.

3.7 Architecture

Our architecture consists of a pre-trained image backbone, a novel image-conditional scene prior diffusion model, and a conditional shape decoder diffusion module. We utilize an off-the-shelf 2D instance segmentation model, Mask2Former [5], which is pre-trained on COCO [36] using a Swin Transformer [39] backbone, to obtain instance segmentation and image features. Please refer to Appendix E for details about the condition embedding functions.

To denoise object poses ρ_i , we use a 1-dim. UNet [55] architecture with 8 encoding and decoding blocks with skip connections. Each block consists of a time-conditional ResNet [18] layer, multi-head attention between the per-object condition y_i and the pose representation, and our intra-scene attention module (Sec. 3.5) to enable relational information exchange and effectively train a scene prior. We use 8 attention heads, with 64 features per head.

To estimate object shapes σ_i from the input view \mathbf{I} , we denoise the unordered set of Gaussian $G_{i,j}$ using a Transformer [69] model with 2 encoder layers, 6 decoder layers, and multi-head attention with 4 heads to the object condition information, similar to [30]. The per-Gaussian latent features are denoised with a shape decoder diffusion model, realized as another Transformer model with 6 encoder and decoder layers, which is conditioned on the shape Gaussians.

3.8 Training and Implementation Details

For all diffusion training processes, we uniformly sample time steps $t = 1, \dots, T, T = 1000$, and use a linear variance schedule with $\beta_1 = 0.0001$ and $\beta_T = 0.02$. We implement our model in PyTorch[50] and use the AdamW [41] optimizer with a learning rate of 1×10^{-4} and $\beta_1 = 0.9, \beta_2 = 0.999$. We train our models on a single RTX3090 with 24GB VRAM for 1000 epochs on Pix3D, for 500 epochs on SUN RGB-D and for 50 epochs of additional joint training using $\mathcal{L}_{\text{align}}$.

During inference, we employ DDIM [61] with 100 steps to accelerate sampling speed. For classifier-free guidance [21], we drop the condition y with probability $p = 0.8$.

4 Experiments

In the following sections, we will demonstrate the advantages of our method and contributions by evaluating it against common 3D scene reconstruction benchmarks.

4.1 Baseline Methods

We compare our method against current state-of-the-art methods for holistic scene understanding: Total3D [48], Im3D [77], and InstPIFu [37]. Total3D [48] directly regresses 3D object poses from image features and uses a mesh deformation and edge-removal approach [49] to reconstruct a shape. Im3D [77] utilizes an implicit shape representation and a graph neural network to refine the pose

predictions. InstPIFu [37] focuses on single-object reconstruction and proposes to query instance-aligned features from the input image in their implicit shape decoder to handle occlusion. For scene reconstruction, they rely on the predicted 3D poses of Im3D. We use the official code and checkpoints provided by the authors of these baseline methods and evaluate with ground truth 2D instance segmentation and camera parameters to ensure a fair comparison. We further compare against a retrieval-based method, ROCA [17] in Appendix D.

4.2 Datasets

Following [23, 48, 77], we train and evaluate the performance of our 3D pose estimation on the SUN RGB-D [62] dataset with the official splits. This dataset consists of 10,335 images of indoor scenes (offices, hotel rooms, lobbies, furniture stores, etc.) captured with four different RGB-D cameras. Each image is annotated with 2D and 3D bounding boxes of objects in the scene. During joint training, we use the provided depth maps together with instance masks to compute $\mathcal{L}_{\text{align}}$.

We train and evaluate the performance of our 3D shape reconstruction on the Pix3D [64] dataset, which contains images of common furniture objects with pixel-aligned 3D shapes from 9 object classes, comprising 10,046 images. We use the train and test splits defined in [37], ensuring that 3D models between the respective splits do not overlap.

4.3 Evaluation Protocol

For quantitative comparison against baseline methods, we follow the evaluation protocol of [48]. For pose estimation, we report the intersection over union of the 3D bounding box ($\text{IoU}_{3\text{D}}$) and average precision with an $\text{IoU}_{3\text{D}}$ threshold of 15% ($\text{AP}_{3\text{D}}^{15}$) on the SUN RGB-D dataset [62]. In line with previous works [48, 77], we evaluate with oracle 2D detections but also provide camera parameters to all methods during evaluation. To further assess the alignment of the 3D shapes in the scene, we calculate $\mathcal{L}_{\text{align}}$ between reconstructed shapes and the instance-segmented ground-truth depth map. For single-view 3D shape reconstruction, we follow evaluate on the Pix3D [64] dataset. We follow [37] and sample 10,000 points on the predicted shape surface, extracted with Marching Cubes [40] at a resolution of 128^3 , and on the ground truth shapes and evaluate Chamfer distance ($\text{CD} \times 10^3$) and F-score after mesh alignment.

4.4 Comparison to State of the Art

3D Scene Reconstruction. In Fig. 3, we present qualitative comparisons of our approach against state-of-the-art methods for single-view 3D scene reconstruction. The results from Total3D often exhibit intersecting objects and lack global structure. Additionally, their deformation and edge-removal approach results in 3D shapes with visible artifacts and limited details. While the implicit shape representation of Im3D is more flexible, it often produces incomplete and floating surfaces. In contrast, our diffusion-based reconstruction method, as shown in Tab. 1, learns strong scene priors, resulting in a +0.2 improvement in $\mathcal{L}_{\text{align}}$ and more coherent 3D arrangements of the objects in the scene (+12.04% $\text{AP}_{3\text{D}}^{15}$), as well as high-quality and clean shapes (+13.43% F-Score).

Furthermore, we demonstrate the generalizability of our model to other indoor datasets. We evaluate our approach on individual frames from the ScanNet [11] dataset using 2D instance predictions from Mask2Former without additional fine-tuning. As shown in Fig. 4, our method accurately reconstructs the given input view with matching poses and high-quality 3D geometries.

In Appendix D, we additionally train on ScanNet and compare against ROCA [17]. Due to its retrieval approach, the shapes are complete. However, the resulting quality can be limited by the diversity of the shape database, which can lead to suboptimal results, see Fig. 11.

3D Pose Estimation & Scene Arrangement. As shown in Tabs. 1 and 6, our method outperforms all baseline methods by a significant margin in terms of $\text{IoU}_{3\text{D}}$ and $\text{AP}_{3\text{D}}^{15}$, *i.e.* `ilet@tokenonedot`, improving $\text{mAP}_{3\text{D}}^{15}$ by 12.04% over Im3D [77]. Detailed per-class results are provided in Tabs. 6 and 8. Figs. 3 and 7 demonstrate that our approach effectively learns common object arrangements, such as multiple chairs surrounding a table, while ensuring that furniture pieces do not intersect or float in the air. We attribute these improvements to our model’s robust scene understanding, which is derived from learning a strong scene prior that accounts for inter-object relationships.

Table 1: **Quantitative evaluation of 3D scene reconstruction on SUN RGB-D [62] (left) and 3D shape reconstruction on Pix3D [64] (right).** Our 3D scene diffusion approach outperforms all baseline methods on both tasks on common 3D scene reconstruction metrics.

	SUN RGB-D [62]						Pix3D [64]			
	IoU _{3D} ↑		AP _{3D} ¹⁵ ↑		L _{align} ↓		CD ↓		F-Score ↑	
Total3D [48]	20.52	(-15.58)	30.56	(-27.62)	1.35	(-0.36)	44.32	(-29.27)	36.20	(-22.51)
Im3D [77]	28.31	(-7.79)	46.14	(-12.04)	1.24	(-0.25)	51.31	(-36.26)	21.45	(-37.26)
InstPiFu [37]	26.14	(-9.96)	45.02	(-13.16)	1.19	(-0.20)	24.65	(-9.6)	45.28	(-13.43)
Ours	36.10		58.18		0.99		15.05		58.71	

Table 2: **Ablations.** We ablate the effect of our contributions and design decisions. We observe significant gains by introducing our proposed scene prior and intra-scene attention module, using denoising diffusion compared to regression, and jointly training shape and pose together.

Diffusion	ISA	Joint	IoU _{3D} ↑		AP _{3D} ¹⁵ ↑		L _{align} ↓	
✗	✓	✗	28.98	(-7.12)	47.10	(-11.08)	1.18	(-0.19)
✓	✗	✗	28.82	(-7.28)	48.88	(-9.30)	1.12	(-0.13)
✓	✓	✗	35.16	(-0.94)	56.07	(-2.11)	1.06	(-0.07)
✓	✓	✓	36.10		58.18		0.99	

3D Object Reconstruction. In Tab. 1, we quantitatively compare the single-view shape reconstruction performance of our approach against baseline methods on the Pix3D dataset. The results demonstrate that modeling single-view reconstruction as conditional generation over a robust shape prior leads to significant improvements in Chamfer Distance (+9.6%) and F-Score (+13.43%). Detailed per-class results can be found in Tabs. 7 and 9. Fig. 9 illustrates that InstPiFu often reconstructs noisy and incomplete shapes. In contrast, our approach produces clean 3D geometries with fine details, such as thin chair legs and the crease between pillows of a sofa.

In Fig. 5, we show unconditional results by injecting \emptyset as a condition (Sec. 3.2), showcasing that our shape prior models detailed and diverse shape modes across several semantic classes. In Fig. 10, we additionally visualize the shape decomposition capabilities resulting from our shape encoding and the scaffolding Gaussian representation.

4.5 Ablations Studies

We conduct a series of detailed ablation studies to verify the effectiveness of our design decisions and contributions. The quantitative results are provided in Tab. 2.

What is the effect of the denoising formulation? To assess the benefits of the denoising diffusion formulation, we construct a 1-step feed-forward regression model that uses the same conditional information as input features and model architecture but regresses the object outputs directly in a single timestep. As shown in Tab. 2, modeling 3D scene reconstruction as a conditional diffusion process, rather than using a feed-forward regression formulation, results in significant improvements of +11.08% AP_{3D}¹⁵ and +0.19 L_{align}.

What is the effect of our scene prior modeling? We evaluate the impact of learning a scene prior by modeling the distribution of all objects and their relationships compared to learning the marginal per-object distribution, *i.e.* `let@tokeneonedot`, predicting each object individually. As shown in Tab. 2, our joint-object scene prior yields a significant improvement of +9.30% AP_{3D}¹⁵ over per-object prediction. This improvement underscores the importance of learning a robust scene prior that effectively captures inter-object relationships.

What is the effect of joint training? We investigate the benefit of joint training for pose and shape using L_{align} compared to individual training of pose estimation and shape reconstruction. Although our model already learns strong scene and shape priors, Tab. 2 shows that joint training provides additional benefits, resulting in an improvement of +2.11% in AP_{3D}¹⁵ and +0.07 in L_{align}.



Figure 3: **Qualitative comparison of 3D scene reconstruction on SUN RGB-D [62].** While the baselines often produce noisy or incomplete shape reconstruction of intersecting or misplaced objects, our method produces plausible object arrangements as well as high-quality shape reconstructions.

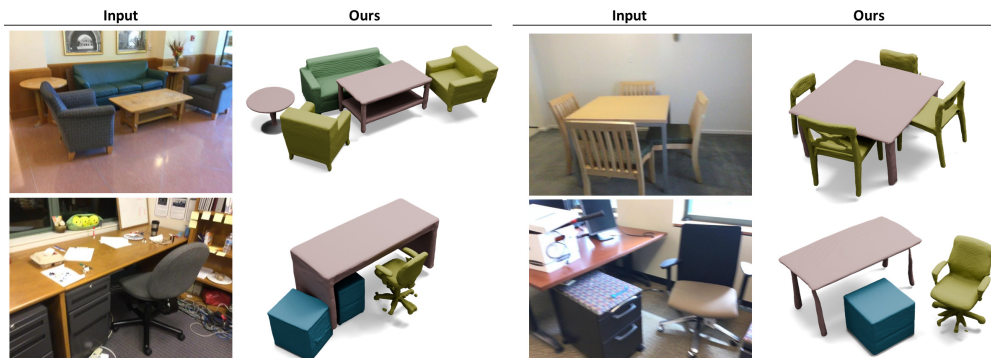


Figure 4: **Inference results on ScanNet [11].** We use our model trained on SUN RGB-D [62] and perform inference on individual frames of ScanNet without fine-tuning. We observe strong generalization capabilities with respect to different camera parameters and scene arrangements.

4.6 Limitations

While our conditional scene diffusion approach for single-view 3D scene reconstruction demonstrates significant improvements, there are some limitations. First, our method relies on accurate 2D object detection, making it dependent on the performance of 2D perception models. Upcoming state-of-the-art 2D detection models [1] can be seamlessly integrated to enhance the performance of our approach. Second, our shape prior, trained on a diverse set of semantic classes using 3D shape supervision, does not generalize to unseen object categories. This can be mitigated by combining our model for known categories with single-object diffusion models that leverage pre-trained text-image generation models for 3D shape synthesis [38] of uncommon shape categories. While accurate 3D scene reconstruction



Figure 5: **Unconditional results.** Injecting \emptyset as a condition to our conditional diffusion model, i.e., effectively disabling the conditioning mechanism, results in high-quality and diverse results.

forms the foundation for subsequent downstream tasks like mixed reality applications, our current model assumes a static scene geometry. Future work could integrate object affordance and articulation into our shape prior [34] to enable more immersive human-scene interactions.

Broader Impact We do not anticipate any societal consequences or negative ethical implications arising from our work. Our approach advances the holistic understanding of 2D perception and 3D modeling, benefiting various research areas.

5 Conclusion

In this paper, we present a novel diffusion-based approach for coherent 3D scene reconstructions from a single RGB image. Our method combines a simple yet powerful denoising formulation with a robust generative scene prior that learns inter-object relationships by exchanging relational information among all scene objects. To address the issue of missing ground-truth annotations in publicly available 3D datasets, we introduce a surface alignment loss $\mathcal{L}_{\text{align}}$ to jointly train shape and pose, effectively leveraging our shape representation. Our approach significantly enhances 3D scene understanding, outperforming current state-of-the-art methods across various benchmarks, with +12.04% $\text{AP}_{3\text{D}}^{15}$ on SUN RGB-D and +13.43% F-Score on Pix3D. Extensive experiments demonstrate that our contributions – 3D scene reconstruction as a conditional diffusion process, scene prior modeling, and joint shape-pose training enabled by $\mathcal{L}_{\text{align}}$ – collectively contribute to the overall performance gain. Additionally, we show that our model supports unconditional synthesis and generalizes well to other indoor datasets without further fine-tuning. We believe these advancements lay a solid foundation for future progress in holistic 3D scene understanding and open up exciting applications in mixed reality, content creation, and robotics.

6 Acknowledgements

This work was funded by the ERC Starting Grant Scan2CAD (804724) of Matthias Nießner and the ERC Starting Grant SpatialSem (101076253) of Angela Dai.

References

- [1] Coco leaderboard. URL <https://cocodataset.org/#detection-leaderboard>.
- [2] A. Alliegro, Y. Siddiqui, T. Tommasi, and M. Nießner. Polydiff: Generating 3d polygonal meshes with diffusion models. *arXiv preprint arXiv:2312.11417*, 2023.
- [3] A. Avetisyan, M. Dahnert, A. Dai, M. Savva, A. X. Chang, and M. Nießner. Scan2cad: Learning cad model alignment in rgb-d scans. In *CVPR*, 2019.
- [4] A. X. Chang, T. Funkhouser, L. Guibas, P. Hanrahan, Q. Huang, Z. Li, S. Savarese, M. Savva, S. Song, H. Su, J. Xiao, L. Yi, and F. Yu. Shapenet: An information-rich 3d model repository. *arXiv preprint arXiv:1512.03012*, 2015.
- [5] B. Cheng, I. Misra, A. G. Schwing, A. Kirillov, and R. Girdhar. Masked-attention mask transformer for universal image segmentation. 2022.
- [6] Y.-C. Cheng, H.-Y. Lee, S. Tulyakov, A. G. Schwing, and L.-Y. Gui. Sdfusion: Multimodal 3d shape completion, reconstruction, and generation. In *Proceedings of the IEEE/CVF Conference on Computer Vision and Pattern Recognition*, pages 4456–4465, 2023.
- [7] G. Chou, Y. Bahat, and F. Heide. Diffusion-sdf: Conditional generative modeling of signed distance functions. 2023.
- [8] C. B. Choy, D. Xu, J. Gwak, K. Chen, and S. Savarese. 3d-r2n2: A unified approach for single and multi-view 3d object reconstruction. In *Computer Vision—European Conference on Computer Vision 2016: 14th European Conference, Amsterdam, The Netherlands, October 11–14, 2016, Proceedings, Part VIII 14*, pages 628–644. Springer, 2016.
- [9] T. Chu, P. Zhang, Q. Liu, and J. Wang. Buol: A bottom-up framework with occupancy-aware lifting for panoptic 3d scene reconstruction from a single image. In *Proceedings of the IEEE/CVF Conference on Computer Vision and Pattern Recognition*, pages 4937–4946, 2023.
- [10] M. Dahnert, J. Hou, M. Nießner, and A. Dai. Panoptic 3d scene reconstruction from a single rgb image. In *Thirty-Fifth Conference on Neural Information Processing Systems*, 2021.
- [11] A. Dai, A. X. Chang, M. Savva, M. Halber, T. Funkhouser, and M. Nießner. Scannet: Richly-annotated 3d reconstructions of indoor scenes. In *CVPR*, 2017.
- [12] M. Deitke, D. Schwenk, J. Salvador, L. Weihs, O. Michel, E. VanderBilt, L. Schmidt, K. Ehsani, A. Kembhavi, and A. Farhadi. Objaverse: A universe of annotated 3d objects. In *CVPR*, 2023.
- [13] Y. Du, Z. Liu, H. Basevi, A. Leonardis, B. Freeman, J. Tenenbaum, and J. Wu. Learning to exploit stability for 3d scene parsing. In *Conference on Neural Information Processing Systems*, 2018.
- [14] H. Fan, H. Su, and L. J. Guibas. A point set generation network for 3d object reconstruction from a single image. In *Proceedings of the IEEE conference on computer vision and pattern recognition*, pages 605–613, 2017.
- [15] G. Gkioxari, J. Malik, and J. Johnson. Mesh r-cnn. In *Proceedings of the IEEE/CVF International Conference on Computer Vision*, 2019.
- [16] T. Groueix, M. Fisher, V. G. Kim, B. Russell, and M. Aubry. AtlasNet: A Papier-Mâché Approach to Learning 3D Surface Generation. In *Proceedings IEEE Conf. on Computer Vision and Pattern Recognition (CVPR)*, 2018.
- [17] C. Gümeli, A. Dai, and M. Nießner. Roca: Robust cad model retrieval and alignment from a single image. 2022.
- [18] K. He, X. Zhang, S. Ren, and J. Sun. Deep residual learning for image recognition. In *Proceedings of the IEEE conference on computer vision and pattern recognition*, pages 770–778, 2016.
- [19] Q. He, D. Zhou, B. Wan, and X. He. Single image 3d object estimation with primitive graph networks. In *Proceedings of the 29th ACM International Conference on Multimedia*, pages 2353–2361, 2021.
- [20] A. Hertz, O. Perel, R. Giryes, O. Sorkine-Hornung, and D. Cohen-Or. Spaghetti: Editing implicit shapes through part aware generation. *ACM Transactions on Graphics (TOG)*, 41(4):1–20, 2022.
- [21] J. Ho and T. Salimans. Classifier-free diffusion guidance. *arXiv preprint arXiv:2207.12598*, 2022.

- [22] J. Ho, A. Jain, and P. Abbeel. Denoising diffusion probabilistic models. *Advances in neural information processing systems*, 33:6840–6851, 2020.
- [23] S. Huang, S. Qi, Y. Xiao, Y. Zhu, Y. N. Wu, and S.-C. Zhu. Cooperative holistic scene understanding: Unifying 3d object, layout, and camera pose estimation. In *Conference on Neural Information Processing Systems*, 2018.
- [24] S. Huang, S. Qi, Y. Zhu, Y. Xiao, Y. Xu, and S.-C. Zhu. Holistic 3d scene parsing and reconstruction from a single rgb image. In *European Conference on Computer Vision*, 2018.
- [25] K.-H. Hui, R. Li, J. Hu, and C.-W. Fu. Neural wavelet-domain diffusion for 3d shape generation. In *SIGGRAPH Asia 2022 Conference Papers*, pages 1–9, 2022.
- [26] H. Izadinia, Q. Shan, and S. M. Seitz. Im2cad. In *CVPR*, 2017.
- [27] W. Jang and L. Agapito. Codenerf: Disentangled neural radiance fields for object categories. In *Proceedings of the IEEE/CVF International Conference on Computer Vision*, pages 12949–12958, 2021.
- [28] T. Karras, M. Aittala, T. Aila, and S. Laine. Elucidating the design space of diffusion-based generative models. *Advances in Neural Information Processing Systems*, 35:26565–26577, 2022.
- [29] S. W. Kim, B. Brown, K. Yin, K. Kreis, K. Schwarz, D. Li, R. Rombach, A. Torralba, and S. Fidler. Neuralfield-ldm: Scene generation with hierarchical latent diffusion models. In *IEEE Conference on Computer Vision and Pattern Recognition (CVPR)*, 2023.
- [30] J. Koo, S. Yoo, M. H. Nguyen, and M. Sung. Salad: Part-level latent diffusion for 3d shape generation and manipulation. In *Proceedings of the IEEE/CVF International Conference on Computer Vision*, pages 14441–14451, 2023.
- [31] N. Kulkarni, I. Misra, S. Tulsiani, and A. Gupta. 3d-relnet: Joint object and relational network for 3d prediction. In *Proceedings of the IEEE/CVF International Conference on Computer Vision*, pages 2212–2221, 2019.
- [32] W. Kuo, A. Angelova, T.-y. Lin, and A. Dai. Mask2cad: 3d shape prediction by learning to segment and retrieve. In *Proceedings of the European Conference on Computer Vision (European Conference on Computer Vision)*, 2020.
- [33] W. Kuo, A. Angelova, T.-Y. Lin, and A. Dai. Patch2cad: Patchwise embedding learning for in-the-wild shape retrieval from a single image. In *Proceedings of the IEEE/CVF International Conference on Computer Vision*, pages 12589–12599, 2021.
- [34] J. Lei, C. Deng, W. B. Shen, L. J. Guibas, and K. Daniilidis. Nap: Neural 3d articulated object prior. In A. Oh, T. Naumann, A. Globerson, K. Saenko, M. Hardt, and S. Levine, editors, *Advances in Neural Information Processing Systems*, volume 36, pages 31878–31894. Curran Associates, Inc., 2023.
- [35] L. Li, S. Khan, and N. Barnes. Silhouette-assisted 3d object instance reconstruction from a cluttered scene. In *2019 IEEE/CVF International Conference on Computer Vision Workshop (Proceedings of the IEEE/CVF International Conference on Computer VisionW)*, pages 2080–2088, 2019. doi: 10.1109/ProceedingsoftheIEEE/CVFInternationalConferenceonComputerVisionW.2019.00263.
- [36] T.-Y. Lin, M. Maire, S. Belongie, J. Hays, P. Perona, D. Ramanan, P. Dollár, and C. L. Zitnick. Microsoft coco: Common objects in context. In *Computer Vision—European Conference on Computer Vision 2014: 13th European Conference, Zurich, Switzerland, September 6–12, 2014, Proceedings, Part V 13*, pages 740–755. Springer, 2014.
- [37] H. Liu, Y. Zheng, G. Chen, S. Cui, and X. Han. Towards high-fidelity single-view holistic reconstruction of indoor scenes. In *European Conference on Computer Vision*, 2022.
- [38] R. Liu, R. Wu, B. V. Hoorick, P. Tokmakov, S. Zakharov, and C. Vondrick. Zero-1-to-3: Zero-shot one image to 3d object. In *Proceedings of the IEEE/CVF International Conference on Computer Vision*, 2023.
- [39] Z. Liu, Y. Lin, Y. Cao, H. Hu, Y. Wei, Z. Zhang, S. Lin, and B. Guo. Swin transformer: Hierarchical vision transformer using shifted windows. In *Proceedings of the IEEE/CVF international conference on computer vision*, pages 10012–10022, 2021.
- [40] W. E. Lorensen and H. E. Cline. Marching cubes: A high resolution 3d surface construction algorithm. *ACM Trans. Gr.*, 21(4):163–169, 1987.

- [41] I. Loshchilov and F. Hutter. Decoupled weight decay regularization. In *International Conference on Learning Representations*, 2018.
- [42] S. Luo and W. Hu. Diffusion probabilistic models for 3d point cloud generation. In *Proceedings of the IEEE/CVF Conference on Computer Vision and Pattern Recognition*, pages 2837–2845, 2021.
- [43] P. Mandikal, N. KL, and R. Venkatesh Babu. 3d-psrnet: Part segmented 3d point cloud reconstruction from a single image. In *Proceedings of the European Conference on Computer Vision (European Conference on Computer Vision) Workshops*, pages 0–0, 2018.
- [44] L. Melas-Kyriazi, C. Rupprecht, and A. Vedaldi. Pc2: Projection-conditioned point cloud diffusion for single-image 3d reconstruction. In *Proceedings of the IEEE/CVF Conference on Computer Vision and Pattern Recognition*, pages 12923–12932, 2023.
- [45] N. Müller, Y. Siddiqui, L. Porzi, S. R. Bulo, P. Kotschieder, and M. Nießner. Diffrf: Rendering-guided 3d radiance field diffusion. In *Proceedings of the IEEE/CVF Conference on Computer Vision and Pattern Recognition*, pages 4328–4338, 2023.
- [46] C. Nash, Y. Ganin, S. A. Eslami, and P. Battaglia. Polygen: An autoregressive generative model of 3d meshes. In *International conference on machine learning*, pages 7220–7229. PMLR, 2020.
- [47] P. K. Nathan Silberman, Derek Hoiem and R. Fergus. Indoor segmentation and support inference from rgb-d images. In *European Conference on Computer Vision*, 2012.
- [48] Y. Nie, X. Han, S. Guo, Y. Zheng, J. Chang, and J. J. Zhang. Total3dunderstanding: Joint layout, object pose and mesh reconstruction for indoor scenes from a single image. In *CVPR*, 2020.
- [49] J. Pan, X. Han, W. Chen, J. Tang, and K. Jia. Deep mesh reconstruction from single rgb images via topology modification networks. In *Proceedings of the IEEE/CVF International Conference on Computer Vision*, 2019.
- [50] A. Paszke, S. Gross, F. Massa, A. Lerer, J. Bradbury, G. Chanan, T. Killeen, Z. Lin, N. Gimelshein, L. Antiga, et al. Pytorch: An imperative style, high-performance deep learning library. In *Conference on Neural Information Processing Systems*, 2019.
- [51] B. Poole, A. Jain, J. T. Barron, and B. Mildenhall. Dreamfusion: Text-to-3d using 2d diffusion. In *ICLR*, 2023.
- [52] S. Popov, P. Bauszat, and V. Ferrari. Corenet: Coherent 3d scene reconstruction from a single rgb image. In *Computer Vision—ECCV 2020: 16th European Conference, Glasgow, UK, August 23–28, 2020, Proceedings, Part II 16*, pages 366–383. Springer, 2020.
- [53] X. Ren, J. Huang, X. Zeng, K. Museth, S. Fidler, and F. Williams. Xcube: Large-scale 3d generative modeling using sparse voxel hierarchies. In *Proceedings of the IEEE/CVF Conference on Computer Vision and Pattern Recognition*, 2024.
- [54] L. Roberts. Machine perception of threedimensional solids. *PhD thesis, Massachusetts Institute of Technology*, 1963.
- [55] O. Ronneberger, P. Fischer, and T. Brox. U-net: Convolutional networks for biomedical image segmentation. In *Medical Image Computing and Computer-Assisted Intervention—MICCAI 2015: 18th International Conference, Munich, Germany, October 5-9, 2015, Proceedings, Part III 18*, pages 234–241. Springer, 2015.
- [56] O. Russakovsky, J. Deng, H. Su, J. Krause, S. Satheesh, S. Ma, Z. Huang, A. Karpathy, A. Khosla, M. Bernstein, et al. Imagenet large scale visual recognition challenge. *International journal of computer vision*, 115:211–252, 2015.
- [57] E. Sella, G. Fiebelman, P. Hedman, and H. Averbuch-Elor. Vox-e: Text-guided voxel editing of 3d objects. In *Proceedings of the IEEE/CVF International Conference on Computer Vision*, pages 430–440, 2023.
- [58] J. R. Shue, E. R. Chan, R. Po, Z. Ankner, J. Wu, and G. Wetzstein. 3d neural field generation using triplane diffusion. In *Proceedings of the IEEE/CVF Conference on Computer Vision and Pattern Recognition*, pages 20875–20886, 2023.
- [59] Y. Siddiqui, A. Alliegro, A. Artemov, T. Tommasi, D. Sirigatti, V. Rosov, A. Dai, and M. Nießner. Meshgpt: Generating triangle meshes with decoder-only transformers. In *Proc. Computer Vision and Pattern Recognition (CVPR), IEEE*, 2024.

- [60] J. Sohl-Dickstein, E. Weiss, N. Maheswaranathan, and S. Ganguli. Deep unsupervised learning using nonequilibrium thermodynamics. In *International conference on machine learning*, pages 2256–2265. PMLR, 2015.
- [61] J. Song, C. Meng, and S. Ermon. Denoising diffusion implicit models. *arXiv preprint arXiv:2010.02502*, 2020.
- [62] S. Song, S. P. Lichtenberg, and J. Xiao. Sun rgb-d: A rgb-d scene understanding benchmark suite. In *CVPR*, 2015.
- [63] S. Song, F. Yu, A. Zeng, A. X. Chang, M. Savva, and T. Funkhouser. Semantic scene completion from a single depth image. *arXiv preprint arXiv:1611.08974*, 2016.
- [64] X. Sun, J. Wu, X. Zhang, Z. Zhang, C. Zhang, T. Xue, J. B. Tenenbaum, and W. T. Freeman. Pix3d: Dataset and methods for single-image 3d shape modeling. In *CVPR*, 2018.
- [65] S. Szymanowicz, C. Rupprecht, and A. Vedaldi. Viewset diffusion: (0-)image-conditioned 3d generative models from 2d data. *International Conference on Computer Vision*, 2023.
- [66] J. Tang, X. Han, J. Pan, K. Jia, and X. Tong. A skeleton-bridged deep learning approach for generating meshes of complex topologies from single rgb images. In *Proceedings of the IEEE/CVF conference on computer vision and pattern recognition*, pages 4541–4550, 2019.
- [67] J. Tang, Y. Nie, L. Markhasin, A. Dai, J. Thies, and M. Nießner. Diffuscene: Scene graph denoising diffusion probabilistic model for generative indoor scene synthesis. *arXiv preprint arXiv:2303.14207*, 2023.
- [68] S. Tulsiani, S. Gupta, D. F. Fouhey, A. A. Efros, and J. Malik. Factoring shape, pose, and layout from the 2d image of a 3d scene. In *Proceedings of the IEEE Conference on Computer Vision and Pattern Recognition*, pages 302–310, 2018.
- [69] A. Vaswani, N. Shazeer, N. Parmar, J. Uszkoreit, L. Jones, A. N. Gomez, L. Kaiser, and I. Polosukhin. Attention is all you need. *Advances in neural information processing systems*, 30, 2017.
- [70] N. Wang, Y. Zhang, Z. Li, Y. Fu, W. Liu, and Y.-G. Jiang. Pixel2mesh: Generating 3d mesh models from single rgb images. In *European Conference on Computer Vision*, 2018.
- [71] J. Wu, C. Zhang, T. Xue, W. T. Freeman, and J. B. Tenenbaum. Learning a probabilistic latent space of object shapes via 3d generative-adversarial modeling. In *Advances in Neural Information Processing Systems*, pages 82–90, 2016.
- [72] H. Xie, H. Yao, X. Sun, S. Zhou, and S. Zhang. Pix2vox: Context-aware 3d reconstruction from single and multi-view images. In *Proceedings of the IEEE/CVF international conference on computer vision*, pages 2690–2698, 2019.
- [73] A. Yu, V. Ye, M. Tancik, and A. Kanazawa. pixelnerf: Neural radiance fields from one or few images. In *CVPR*, 2021.
- [74] X. Zeng, A. Vahdat, F. Williams, Z. Gojcic, O. Litany, S. Fidler, and K. Kreis. Lion: Latent point diffusion models for 3d shape generation. *arXiv preprint arXiv:2210.06978*, 2022.
- [75] B. Zhang, M. Nießner, and P. Wonka. 3DILG: Irregular latent grids for 3d generative modeling. In *Thirty-Sixth Conference on Neural Information Processing Systems*, 2022.
- [76] B. Zhang, J. Tang, M. Niessner, and P. Wonka. 3dshape2vecset: A 3d shape representation for neural fields and generative diffusion models. *arXiv preprint arXiv:2301.11445*, 2023.
- [77] C. Zhang, Z. Cui, Y. Zhang, B. Zeng, M. Pollefeys, and S. Liu. Holistic 3d scene understanding from a single image with implicit representation. In *CVPR*, 2021.
- [78] X. Zhang, Z. Chen, F. Wei, and Z. Tu. Uni-3d: A universal model for panoptic 3d scene reconstruction. In *Proceedings of the IEEE/CVF International Conference on Computer Vision (Proceedings of the IEEE/CVF International Conference on Computer Vision)*, pages 9256–9266, October 2023.
- [79] X. Zheng, Y. Liu, P. Wang, and X. Tong. Sdf-stylegan: Implicit sdf-based stylegan for 3d shape generation. In *Computer Graphics Forum*, volume 41, pages 52–63. Wiley Online Library, 2022.
- [80] L. Zhou, Y. Du, and J. Wu. 3d shape generation and completion through point-voxel diffusion. In *Proceedings of the IEEE/CVF International Conference on Computer Vision*, pages 5826–5835, 2021.

A Appendix

In the following, we show more qualitative results for scene reconstruction on SUN RGB-D [62] (Appendix B) and object reconstruction on Pix3D [64]. We provide detailed quantitative per-class comparisons supplementing the tables in the main paper (Appendix C). We additionally compare against a retrieval baseline on the ScanNet [11] dataset in Appendix D. Finally, we provide additional details on the architecture of our diffusion model in (Appendix E).

For a comprehensive overview of our approach and results, we encourage the reader to watch the supplemental video.

B Additional Qualitative Results

Scene Reconstruction In Fig. 6, we show additional qualitative results of our method on test frames from SUN RGB-D. Despite strong occlusions and challenging viewing angles, our model predicts accurate scene reconstructions. Our generative scene prior learns common scene patterns, such as parallel object placements between the table and sofa or a bed and neighboring nightstands. In Fig. 8, we also demonstrate that our robust conditional scene prior can recover clean and matching shape reconstruction even for heavily occluded objects, *e.glet@tokenonedot*, a chair for which only the back seat is barely visible.

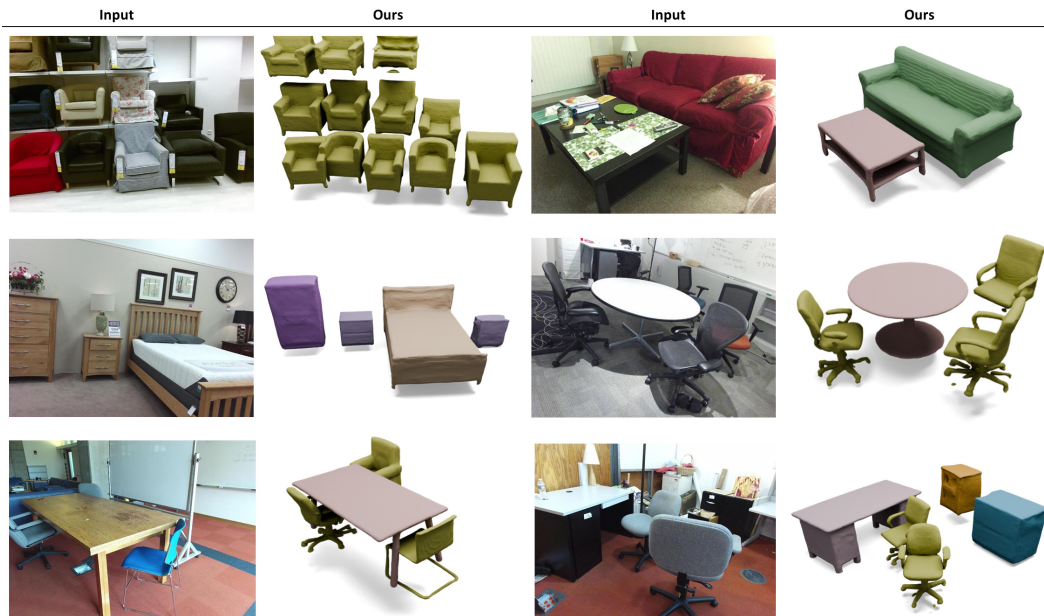


Figure 6: **Additional qualitative scene reconstruction results on SUN RGB [62]**. Our diffusion-based scene layout and shape prediction approach achieves accurate results even for strongly occluded objects.

Object Reconstruction & Unconditional Synthesis In Fig. 9, we show a qualitative comparison of single-view 3D object reconstruction on the Pix3D dataset. Unlike InstPIFu, which often produces noisy and incomplete surfaces, our image-condition diffusion model reconstructs clean and high-fidelity objects. Such a visual quality allows these reconstructions to be integrated into *e.glet@tokenonedot*, mixed reality applications.

To probe the learned shape prior and investigate its shape synthesis capabilities, we input the 0-condition \emptyset instead of extracted image features to our model. As shown in Fig. 5, our model learns a high-quality shape prior with fine details across various semantic classes.



Figure 7: **Qualitative comparison of 3D pose estimation on the SUN RGB-D [62].** The input image is displayed on the left, and the predicted and ground-truth 3D arrangements are visualized as top-down orthographic views of the scene. We observe that Total3D frequently lacks a globally consistent structure, while Im3D predicts globally structured results but occasionally produces intersecting or floating objects. In contrast, our approach successfully recovers a coherent arrangement of objects within the scene by learning a robust scene prior.

C Additional Quantitative Results

Scene Reconstruction In Tab. 4, we show detailed comparisons of our approach against baseline methods, Total3D [48] and Im3D [77], on the 10 most common classes of SUN RGB-D. Our approach consistently outperforms all baseline methods on all classes except the “bed” class. We attribute this exception to the fact that beds are often only partially visible in the input view due to their spatial extent, which introduces higher variability. In contrast, Im3D employs a series of geometric losses and regularization terms, which seems to help in extreme amodal cases at the cost of additional loss balancing. Nevertheless, our method achieves a significant overall improvement of 12.04% in AP_{3D}^{15} on these 10 classes, with particularly notable gains for “dressers” (+26.03%), “chairs” (+21.91%) and “cabinets” (+19.37%), showcasing the effect of our robust scene prior.

Tabs. 6 and 8 show the per-class comparisons and ablation studies on all 37 NYU classes in terms of IoU_{3D} and mAP_{3D}^{15} . Our approach improves compared to Im3D by a +7.57% increase in mAP_{3D}^{15} and +4.56% increase in class-mean IoU_{3D} across all 37 classes. The ablation results highlight the importance of our diffusion formulation (+7.67% mAP_{3D}^{15}), scene prior modeling (+7.11% mAP_{3D}^{15}), and joint training using the surface alignment loss \mathcal{L}_{align} (+0.72 mAP_{3D}^{15}).

Object Reconstruction For single-view object reconstruction, we evaluate Chamfer Distance and F-Score on Pix3D and show per-class comparisons in Tabs. 7 and 9. Our image-conditional shape prior leads to significant improvements, +9.6% in Chamfer Distance and +13.43 in F-Score, while outperforming InstPIFu in most categories, except sofas and wardrobes in F-Score.

Room Layout [48, 77] also predict the room bounding box with a separate network head. We study, how our model can also predict the room layout. For that we include the room bounding

box pose as part of the object poses during the diffusion process. We follow the room layout parameterization of [48, 77] and model the 3D room center directly instead of decomposing it as 2D offset & distance, which is done for the objects. In Tab. 3, we demonstrate that by denoising the pose of room layout, we outperform the regression-based methods.

Table 3: **Additional 3D room layout estimation on SUN RGB-D [62]**. We evaluate the 3D IoU of the orientied room bounding box. Our diffusion-based pose estimation lead to an improvement of +1.7% in Room Layout IoU.

	Layout IoU
Total3D [48]	59.2
Im3D [77]	64.4
Ours	66.1

Table 4: **Additional per-class comparisons of 3D layout estimation on SUN RGB-D [62]**. Our method outperforms the baselines in most categories with overall strong improvements in mAP_{3D} evaluated at an IoU-threshold of 15%.

	bed	chair	sofa	table	desk	dresser	n.stand	sink	cabinet	lamp	mAP_{3D}^{15}
Total3D [48]	72.47	22.74	53.56	41.49	32.74	17.45	20.06	24.67	16.83	3.63	32.54
Im3D [77]	88.73	36.77	72.81	58.64	49.80	29.73	44.10	34.71	32.72	13.34	46.14
Ours	86.58	58.68	74.13	71.36	62.81	55.76	48.14	50.44	52.09	21.82	58.18

Table 5: **Quantitative comparison with ROCA [17] on the ScanNet dataset [11]**. While ROCA estimated each object’s pose individually, our generative scene prior can reason about object relationships, leading to a +3.1% improvement in class-wise alignment accuracy.

	bathtub	bed	bin	b.shelf	cabinet	chair	display	sofa	table	cls.	inst.
ROCA [17]	22.5	10.0	29.3	14.2	15.8	41.0	30.9	16.8	14.5	21.7	27.4
Ours	28.7	18.3	19.1	17.6	36.9	39.7	19.2	24.5	19.2	24.8	29.5

D Comparison to shape retrieval baseline on ScanNet

We compare with a shape retrieval baseline, namely ROCA [17]. Since ROCA requires full ground-truth supervision during training, we adopt their setup and train our model on the same 25,000 frames from the ScanNet [11] dataset with pose annotations derived from Scan2CAD [3], as well as the same CAD pool from ShapeNet [4]. We additionally adopt their full 9-DoF pose parameterization by predicting all 3 rotation angles. Following ROCA, we quantitatively evaluate the Alignment Accuracy in Tab. 5. Please refer to [3, 17] for the details of the evaluation. In Fig. 11, we can see that ROCA retrieves clean and complete shapes by definition. However, due to its limited shape database, it cannot capture all shape modes accurately, leading to shape mismatches. Our reconstruction-based approach instead can recover faithful shape results while simultaneously predicting a coherent object arrangement.

E Architecture Details

Object Pose Parameterization: Normalization To ensure a reasonable signal-noise ratio [28] among the object pose parameters, we normalize the parameters to $[-1, 1]$ by dividing them by its max value and shift the range using a parameter-specific μ value. For this, we calculate the min-max ranges of all pose parameters, $i.elet@tokeneonedot$, rotation θ , 3D scale s , and projected distance d ,

Table 6: **3D pose estimation results** for all NYU-37 classes on SUN RGB-D [62]. We report the Average Precision (AP) at 15% 3D-IoU threshold of the baseline and different variants of our approach: Our approach outperforms Total3D and Im3D on most semantic categories, especially on frequent classes likes chairs (+21.9%) or tables (+12.7%).

	Total3D	Im3D	Ours					full
			no M2F	no diff.	no ISA	no joint	full	
<u>cabinet</u>	16.83	32.72	35.43	37.32	40.48	48.48	52.09	
<u>bed</u>	72.47	88.73	76.23	84.58	86.50	90.71	86.58	
<u>chair</u>	22.74	36.77	46.97	49.38	48.82	55.80	58.68	
<u>sofa</u>	53.56	72.81	64.83	66.44	66.27	72.43	74.13	
<u>table</u>	41.49	58.64	62.31	59.34	58.47	69.70	71.36	
door	1.18	5.85	6.25	3.58	5.58	7.73	5.44	
window	2.72	0.57	0.51	3.08	2.57	2.62	2.72	
bookshelf	4.95	18.02	19.56	25.07	20.99	30.81	30.81	
picture	1.21	1.66	0.99	2.04	1.31	1.80	3.95	
counter	41.29	62.48	62.58	62.30	56.47	69.78	72.44	
blinds	0.00	2.79	1.67	2.27	3.64	4.27	5.20	
<u>desk</u>	32.74	49.80	52.31	48.78	48.93	60.20	62.81	
shelves	9.72	18.16	14.58	16.31	14.51	25.31	28.01	
curtain	1.30	7.69	9.19	3.94	6.76	11.93	10.43	
<u>dresser</u>	17.45	29.73	36.07	41.86	50.91	53.06	55.76	
pillow	9.41	19.48	19.37	23.10	20.54	33.45	28.99	
mirror	0.50	0.84	4.22	1.11	2.04	8.15	9.98	
clothes	0.00	0.00	0.0	0.00	0.00	0.00	0.0	
books	4.23	7.16	5.42	11.26	10.73	17.18	12.76	
fridge	25.00	40.47	27.13	42.66	37.59	45.90	46.17	
television	10.88	14.49	13.89	11.95	10.71	19.81	23.55	
paper	3.47	1.14	1.97	4.96	4.75	4.97	5.75	
towel	4.35	14.80	2.68	8.11	8.19	11.02	12.99	
s.curtain	0.00	0.00	0.00	0.00	0.00	0.00	0.00	
box	7.40	11.52	15.86	17.43	17.72	29.02	24.42	
whiteboard	1.40	2.59	2.68	1.66	3.17	4.18	5.44	
person	22.12	19.22	38.32	31.48	28.45	55.10	56.39	
<u>nightstand</u>	20.06	44.10	28.76	38.41	36.32	45.50	48.14	
<u>toilet</u>	64.36	73.14	65.11	61.56	71.57	71.19	66.30	
<u>sink</u>	24.67	34.71	30.49	32.01	39.60	42.94	50.44	
<u>lamp</u>	3.63	13.34	12.90	12.88	12.48	21.84	21.82	
<u>bathtub</u>	46.86	66.54	30.51	36.47	40.87	50.46	52.77	
bag	13.67	8.45	8.66	13.78	16.52	18.89	21.69	
mAP _{3D} ¹⁵ (all)	17.63	26.01	24.17	25.91	26.47	32.86	33.58	
mAP _{3D} ¹⁵ (10/37)	30.56	46.14	44.63	47.10	48.88	56.07	58.18	

within the train set of SUN RGB-D. The 2D offsets to the 2D bounding box center are normalized by the image dimensions.

$$\mathbf{d} : \mu = 2.7, \max = 2.5, \tag{12}$$

$$\mathbf{s} : \mu = 3.5, \max = 7.0, \tag{13}$$

$$\theta : \mu = 0.0, \max = 3.14. \tag{14}$$

During training, the loss is computed on the un-normalized parameter ranges. After inference and for evaluation, we un-normalize each parameter according to its original range.

Surface Alignment Loss: Point Sample Transformation During training, for each object o_i , we use the predicted shape $\hat{\sigma}_i$ to estimate its scaffolding Gaussians \hat{G}_j . From each 3D Gaussian distribution, we directly draw 3D point samples $p_{(j,t)} \sim \mathcal{N}(\mu_j, \Sigma_j)$. This shape point cloud P_i approximates the shape. With the predicted and un-normalized object pose $\hat{\rho}_i$, we define a 3D rigid transformation $\mathcal{R}^{4 \times 4}$ and transform the shape point cloud P_i to the camera coordinate system. We use this transformed shape pointcloud P_i^{cam} and the instance-segmented ground-truth depth map from

Table 7: **Per-class comparisons of shape reconstruction on Pix3D [64]**. We report F-Score using the non-overlapping 3D model split from [37]. We observe noticeable improvements or comparable results on all categories.

	bed	b.case	chair	desk	misc	sofa	table	tool	w.robe	F-Score
Total3D [48]	34.69	28.42	35.67	34.90	10.41	51.15	17.05	57.16	52.04	36.20
Im3D [77]	37.13	15.51	25.70	26.01	11.04	49.71	21.16	5.85	59.46	31.45
InstPIFu [37]	54.99	62.26	35.30	47.30	27.03	56.54	37.51	64.24	94.62	45.62
Ours	62.47	65.32	60.05	56.67	30.89	55.87	56.28	69.11	92.56	58.71

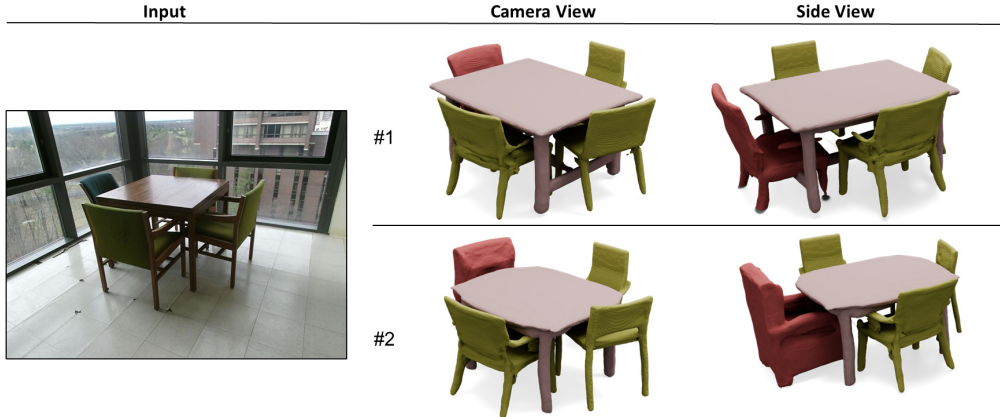


Figure 8: **Probabilistic behavior for partially occluded shapes**. In the input image, the left chair is heavily occluded, which allows for multiple plausible interpretations of the non-visible part of the shape. Our diffusion-based method derives faithful modes.

SUN RGB-D as the partial target pointcloud to measure the 1-sided Chamfer distance and to compute the surface alignment loss $\mathcal{L}_{\text{align}}$.

Scene Prior Modeling: Inter-Object Relationships via Intra-Scene Attention We use the multi-head attention mechanism [69] between the scene objects to allow them to attend to each other, effectively learning their inter-object relationships and the scene context. Specifically, given an unordered set $S = [o_1, o_2, \dots, o_n]$, $o_i \in \mathcal{R}^n$ per-object n -dimensional feature vectors, projection layers (W^Q , W^K and W^V) and features $Q = S \times W^Q$, $K = S \times W^K$ and $V = S \times W^V$ after projection. we define the intra-scene attention as:

$$ISA(S) = softmax\left(\frac{QK^T}{\sqrt{d_d}}\right)V \quad (15)$$

Condition: Embedding Functions After cropping the 2D image feature patch $\mathcal{R}^{W \times H \times C}$ from the frozen image backbone Θ_1 , we apply adaptive average pooling to resize the per-object feature patches to a common 2D size leading to resized per-object feature crop of 8×8 and $C = 256$. This feature crop is further embedded using a small 2D CNN Θ_{feat} with 3 blocks of convolutional layers with 512 features, group norm, and leaky ReLU activation. The embedded feature crop is reshaped to a 4096-dim vector.

Θ_{box} is implemented as sinusoidal position encoding with 10 frequencies. This function is applied on a 2D bounding box, represented by the top-left and bottom-right corners, leading to an 84-dim vector per object. For Θ_{cls} , we use a simple 1-hot encoding to embed the semantic class information. The final per-object condition information is the concatenation, resulting in a 4127-dim vector for each object.

Reimplementation of SPAGHETTI [20] Since the official code of SPAGHETTI does not include the training code and only provides checkpoints for two different shape classes (chairs,

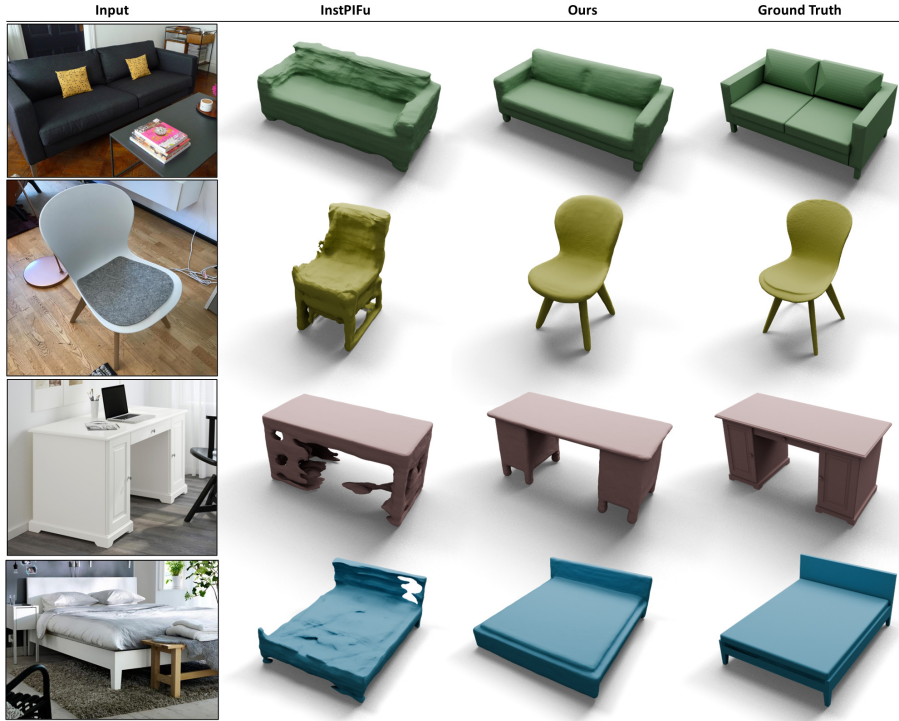


Figure 9: **Qualitative comparison of 3D shape reconstruction on the Pix3D [64].** While InstPIFu often produces noisy surfaces, our image-conditional 3D diffusion model synthesizes high-quality shapes that closely match the target geometries.

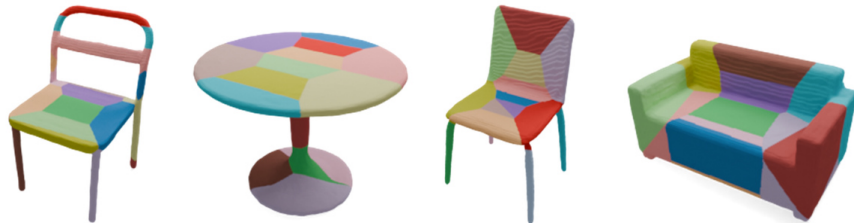


Figure 10: **Shape decomposition visualization.** We assign each vertex of the reconstructed mesh to the closest 3D Gaussian center and visualize the assignment with individual colors. Our scaffolding representation decomposes the shape into distinctive regions and aligns well with certain semantic parts, e.g., individual chair legs or the arm rests of a sofa.

airplanes), we re-implement the training procedure, loss function, and disentanglement loss following the description in the papers to train the full shape prior over all relevant shape categories. Random geometric augmentations are essential during training to achieve self-supervised disentanglement into extrinsic and intrinsic shape properties. We apply full 360-degree random rotations, uniform scale augmentation between 0.7 and 1.3, and translation jitter of ∓ 0.3 on the disentangled extrinsic and target pointcloud. Further, we do not utilize the symmetry options of the original implementation.

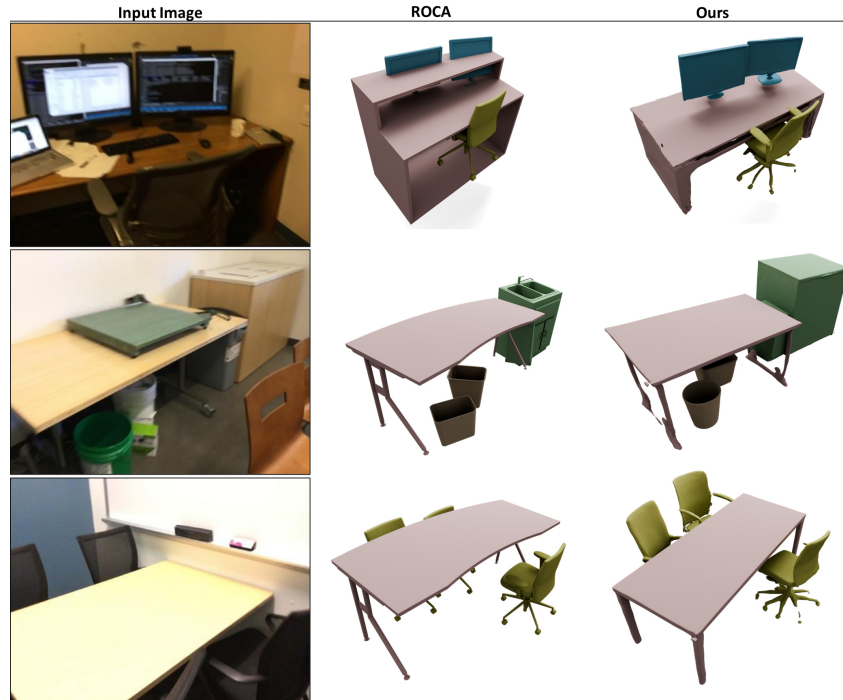


Figure 11: Comparison with retrieval baseline method ROCA [17] on frames from ScanNet [11]. While ROCA cannot always retrieve a matching mode from the shape database, such as the desk in the first row, our diffusion-based reconstruction approach reconstructs accurate shapes and poses.

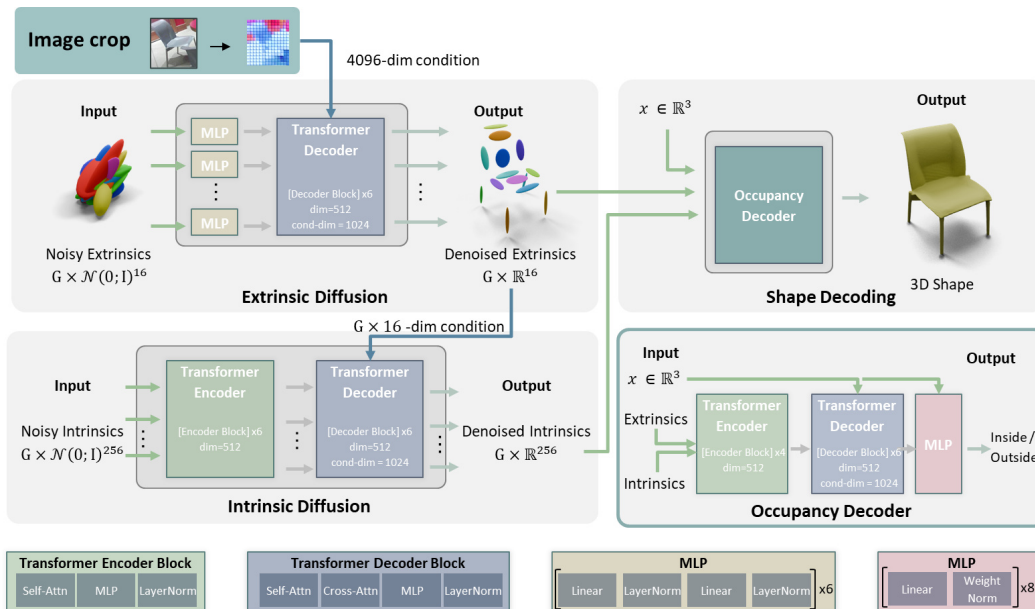


Figure 12: **Architecture Diagram of the Shape Diffusion Model.** The shape diffusion model consists of 3 sub-parts: An image-conditioned diffusion model, denoising the 3D Gaussians; a 3D Gaussian-conditioned diffusion model, denoising the intrinsic vectors; and an Occupancy Decoder, which takes as input a 3D point coordinate and the denoised extrinsics & intrinsic and outputs an occupancy value indicating whether the 3D point is inside/outside of the shape.

Table 8: **Per-class pose estimation results** for all NYU-37 classes on SUN RGB-D [62]. We evaluate the pose estimation quality in terms of 3D IoU. Our scene prior formulation achieves improvements across all categories which particular high gains on common object classes like “chair” (+16.6%) or “desk” (+16.4%).

	Total3D	Im3D	Ours				
			no M2F	no diff.	no ISA	no joint	full
cabinet	13.68	21.96	23.16	26.06	24.54	33.07	32.97
bed	32.28	42.65	41.53	48.98	44.87	52.67	52.25
chair	19.85	26.87	30.62	33.94	30.97	42.92	43.52
sofa	28.32	36.00	32.98	32.69	34.91	38.72	39.48
table	25.70	33.74	32.55	30.41	32.31	40.11	39.95
door	3.91	7.84	7.35	10.01	7.76	10.33	6.73
window	3.52	2.65	2.10	3.12	6.86	15.45	18.17
bookshelf	9.07	16.76	17.16	16.75	18.15	24.45	19.43
picture	2.35	5.30	4.69	5.70	4.32	3.36	6.32
counter	21.72	26.82	30.87	28.25	30.92	42.56	38.43
blinds	1.90	7.11	8.38	0.00	5.53	0.00	0.00
desk	21.09	28.21	28.12	34.57	27.51	44.22	44.68
shelves	10.33	14.92	14.01	16.35	14.81	24.32	17.60
curtain	5.09	9.46	10.40	7.99	9.39	2.55	0.00
dresser	16.84	23.29	23.08	22.86	27.82	29.19	32.56
pillow	11.07	17.65	16.62	18.12	16.77	19.05	16.69
mirror	2.05	4.45	5.65	4.83	4.11	9.03	5.81
clothes	0.00	0.00	0.00	0.00	0.00	0.00	0.00
books	6.81	8.97	9.59	14.00	15.63	12.30	20.48
fridge	18.41	27.02	19.92	16.18	24.61	26.85	23.36
television	9.59	14.11	12.74	12.60	11.62	19.73	18.93
paper	5.16	4.86	8.76	8.10	17.11	12.54	10.40
towel	7.46	10.53	7.26	10.83	8.32	18.79	13.71
s.curtain	33.12	13.49	30.53	0.00	0.00	0.00	9.41
box	9.40	12.04	16.18	17.91	16.47	24.55	23.82
whiteboard	4.06	6.27	5.94	4.07	6.39	6.46	5.47
person	24.14	23.33	28.94	15.40	21.89	19.50	28.91
nightstand	17.93	29.12	21.06	25.80	24.92	25.59	24.81
toilet	34.11	39.46	38.15	28.95	39.63	51.58	50.91
sink	19.92	25.40	21.50	20.54	24.99	20.81	26.60
lamp	9.63	15.90	12.92	13.94	13.20	24.33	24.22
bathtub	24.64	29.56	24.06	27.38	24.80	34.26	35.17
bag	11.18	11.70	13.63	18.41	16.38	22.74	21.60
mIoU _{3D} (all)	14.15	18.10	18.53	17.30	18.76	22.79	22.66
mIoU _{3D} (10/37)	20.52	28.31	26.75	28.98	28.82	35.16	36.10

Table 9: **Per-class comparisons of shape reconstruction on Pix3D [64]**. We report Chamfer Distance using the non-overlapping 3D model split from [37]. Across most categories, our model achieves strong improvements compared to the baselines. Especially for frequent classes like “chair” or “table”, we see a reduction of more than 45%.

	bed	b.case	chair	desk	misc	sofa	table	tool	w.robe	CD
Total3D [48]	22.91	36.61	56.47	33.95	137.50	9.27	81.19	94.70	10.43	44.32
Im3D [77]	11.88	29.61	40.01	65.36	144.06	10.54	146.13	29.63	4.88	51.31
InstPIFu [37]	10.90	7.55	32.44	22.09	47.31	8.13	45.82	10.29	1.29	24.65
Ours	8.43	7.11	17.63	19.81	65.29	8.41	21.06	8.07	2.01	15.05